Transient behavior between multi-cell flow states in ferrofluidic Taylor-Couette flow

Sebastian Altmeyer, Younghae Do, and Soorok Ryu

Transient behavior between multi-cell flow states in ferrofluidic Taylor-Couette flow

Sebastian Altmeyer,[1,2] Younghae Do,[3,a)] and Soorok Ryu[3]

[1]*Castelldefels School of Telecom and Aerospace Engineering, Universitat Politècnica de Catalunya, 08034 Barcelona, Spain*
[2]*Institute of Science and Technology Austria (IST Austria), 3400 Klosterneuburg, Austria*
[3]*Department of Mathematics, KNU-Center for Nonlinear Dynamics, Kyungpook National University, Daegu 41566, South Korea*

We investigate transient behaviors induced by magnetic fields on the dynamics of the flow of a ferrofluid in the gap between two concentric, independently rotating cylinders. Without applying any magnetic fields, we uncover emergence of flow states constituted by a combination of a localized spiral state in the top and bottom of the annulus and different multi-cell flow states with toroidally closed vortices in the interior of the bulk. However, when a magnetic field is presented, we observe the transient behaviors between multi-cell states passing through two critical thresholds in a strength of an axial (transverse) magnetic field. Before the first critical threshold of a magnetic field strength, multi-stable states with different number of cells could be observed. After the first critical threshold, we find the transient behavior between the three- and two-cell flow states. For more strength of magnetic field or after the second critical threshold, we discover that multi-cell states are disappeared and a localized spiral state remains to be stimulated. The studied transient behavior could be understood by the investigation of various quantities including a modal kinetic energy, a mode amplitude of the radial velocity, wavenumber, angular momentum, and torque. In addition, the emergence of new flow states and the transient behavior between their states in ferrofluidic flows indicate that richer and potentially controllable dynamics through magnetic fields could be possible in ferrofluic flow. *Published by AIP Publishing.* https://doi.org/10.1063/1.5002771

We investigate the transient behaviors induced by magnetic fields on ferrofluidic Taylor-Couette system by solving the ferrohydrodynamical equations, carrying out systematic analysis of various quantities. Without applying any magnetic fields, multi-stable flow states can be observed, which are constituted by a combination of a localized spiral state (SPI$_l$) in the top and bottom of the annulus and different multi-cell flow states (SPI$_{2v}$, SPI$_{3v}$) with toroidally closed vortices in the interior of the bulk (SPI$_{l+2v}$ = SPI$_l$ + SPI$_{2v}$ and SPI$_{l+3v}$ = SPI$_l$ + SPI$_{3v}$). However, when a magnetic field is applied, two transient behaviors between multi-cell states can be observed. For stronger magnetic field or after the second critical threshold, we find that multi-cell states are disappeared and only a localized spiral state is more stimulated, which can be supported through investigation of various quantities.

I. INTRODUCTION

The study of flow confined between two concentric differentially rotating cylinders, the Taylor-Couette system (TCS), has played a central role in understanding the various hydrodynamic stabilities.[1,2] TCS has been a paradigm to investigate many fundamental nonlinear dynamical phenomena in fluid flows. Due to the simplicity of the geometry of TCS, well-controlled experimental studies are also possible.

Thus, the vast literature in this area has been built on the TCS with a simple fluid. Recently, there has been an increasing amount of interest in the flow dynamics of the TCS with a complex fluid.[2–6] One of a representative complex fluids is ferrofluids,[7] which are manufactured fluids consisting of dispersion of magnetized nanoparticles in a liquid carrier and also can be stabilized against agglomeration through the addition of a surfactant monolayer onto the magnetic particles.

In the absence of any magnetic field, the nanoparticles are randomly oriented so that the fluid has zero net magnetization. It means that the nanoparticles alter little the viscosity and the density of the fluid. Therefore, a ferrofluid without having any external field behaves as a simple (classical) fluid. However, when a magnetic field of sufficient strength is applied, the hydrodynamical properties of the fluid, such as the viscosity, can be changed dramatically[8–11] and the dynamics can be drastically altered. For instance, under a symmetry-breaking transverse magnetic field, all flow states in the TCS become intrinsically three-dimensional.[11–13] Thus, the study of a ferrofluid in TCS has attracted attention in recent years.[10–23]

A recent study shows that a magnetic field can have a significant influence on the hydrodynamical stability and the underlying symmetries of the flow states through, for example, certain induced azimuthal modes,[11,13] and a change in the magnetic field strength can also induce chaotic behavior and turbulence.[22] Ferrofluidic flows have wide applications, ranging from gaining insights into the fundamentals of geophysical flows through laboratory experiments[24,25] to the

a)yhdo@knu.ac.kr

development of microfluidic devices and computer hard drives.

The present study of flow states in the ferrofluidic TCS considers finite length annulus and co-rotating cylinders. So far, the latter has been studied mainly with a focus on non-linear pattern formation,[5,26,27] as well with an emphasis on magnetohydrodynamical phenomena with respect to astro-physical application[28,29] and in turbulent flows.[30,31] In particular, turbulence in ferrofluidic Taylor-Couette flow has been recently studied, for the first time.[22] In the context of astrophysical application, there have been some attempts to quantitatively reduce the boundary-driven circulation by rotating endwalls.[32,33] However, (stationary) endwalls are absolutely *evident* and remain an integral part of the physical realization of Taylor-Couette flow that qualitatively differs in bifurcation behavior from circular Couette flow.[34–37] In the co-rotating flow regime with infinite cylinders, circular Couette flow[1] becomes centrifugally unstable and axisymmetric toroidally closed cells (Taylor vortices)[1] appear. Moreover, depending on the system parameters localized spiral states exist.[5,36,38] The classical TCS offers a wide variety and multiplicity of multi-cell states, which can either be time-dependent or time-independent. Typical representatives of the latter are the stationary cellular states.[39] However, more interesting in general due to its increased complexity is the time-dependent flow states. One type of this class is the axisymmetric propagating vortices,[40] which appear in the centrifugally stable regime of counter-rotating Taylor-Couette flow. In contrast to propagating spiral vortices, which are non-axisymmetric rotating waves, these axisymmetric propagating vortices are time-dependent in any rotating frame and reflection symmetry is revealed.

In this paper, we report the emergence of new two flow states and transient behavior between them through a systematic computational study of flow dynamics of ferrofluidic Taylor-Couette flow in *co-rotating* regime, having a finite system length with stationary endwalls for moderate to large aspect ratio (cylinder length/gap width) of about ten. [The radius ratio of the cylinders (inner cylinder radius/outer cylinder radius) is fixed to 0.5.] Specifically, we set the rotation speeds of the inner and outer cylinders so as to fix its Reynolds number ($Re_{1,2} = \omega_{1,2} r_2 d/\nu$) at $Re_1 = 247$ and $Re_2 = 110$. To distinguish from the dynamics of a simple fluid, *axial* magnetic field and a symmetry breaking *transverse* magnetic field are applied. Thus, the transverse or axial magnetic field strength, respectively, is chosen as a bifurcation parameter, and we focus on their influence to the global boundary-driven circulation in the annulus.

The main results can be stated as follows. We find the flow states that are constituted by a combination of local flow states: a localized spiral state (SPI_l) in the top and bottom of the annulus and different multi-cell flow states (SPI_{2v}, SPI_{3v}) with toroidally closed vortices in the interior of the bulk, that is, $SPI_{l+2v} = SPI_l + SPI_{2v}$ and $SPI_{l+3v} = SPI_l + SPI_{3v}$. However, when a magnetic field is presented, we observe two transient behaviors, that is, passing through two critical thresholds in a strength of an axial (transverse) magnetic field. The first transient behavior happens between multi-cell states, and the second transition for between multi-cell state and a localized spiral

state. Before the first transition happens, two flow states SPI_{l+2v} and SPI_{l+3v} are coexisted, which are depending on initial conditions. For more strength of magnetic field or after the second critical threshold, only a localized spiral state SPI_l is more stimulated and multi-cell states are disappeared. But, depending on the field orientation, there is a significant difference in a localized spiral location: the interior bulk region for an axial magnetic field and the Ekman boundary-layer region for a transverse magnetic field, which can be observed through a change in multi-cell states by increasing s_x and s_z, respectively.

The interesting observation is that there are favorable states for magnetic fields: SPI_{2V} (SPI_{3V}) in case of axial (transverse) oriented fields. However, enough strong magnetic fields, independent of its orientation, destroy all multi-cell flow states and leave pure SPI_l states. More interesting is that the propagation direction of a SPI_l is also depending on magnetic fields. We note that the symmetry breaking effect of the transverse magnetic field (a stimulated two-cell mode[12,37,41]) only plays a minor role in the present study.

For the here studied aspect ratio ($\Gamma = 10$), we find two local flow states (SPI_{2V}, SPI_{3V}) with two or three toroidally closed vortex pairs aside the SPI_l. However, for larger Γ, we note that more pairs of vortices can be observed in the system. All flow states with or without the small toroidally closed vortices are inherently three dimensional. It indicates that all flow states are stimulated by various azimuthal and non-axisymmetric $m \neq 0$ modes, incorporating a large number of azimuthal modes.

In Sec. II, we describe the ferrofluidic system and numerical method. In Sec. III, we present our main results: the coexisting flow states in absence of a magnetic field, transient dynamics in the present of magnetic fields, and changes in various quantities through transient behavior. Finally, we present conclusions and discussions in Sec. IV.

II. SYSTEM SETTING AND THE NAVIER-STOKES EQUATION

We consider a standard TCS consisting of two independently rotating cylinders. Within the gap between the two concentric cylinders there is an incompressible, isothermal, homogeneous, and mono-dispersed ferrofluid of kinematic viscosity ν and density ρ. The inner and outer cylinders have radius R_1 and R_2, and they rotate with the angular velocity ω_1 and ω_2, respectively. The boundary conditions at the cylinder surfaces are of the non-slip type, and the end walls enclosing the annulus are stationary. The system can be characterized in the cylindrical coordinate system (r, θ, z) by the velocity field $\mathbf{u} = (u, v, w)$ and their corresponding vorticity field $\nabla \times \mathbf{u} = (\xi, \eta, \zeta)$. We fix the radius ratio $R_1/R_2 = 0.5$ of the cylinders and the height-to-gap aspect ratio $\Gamma = 10$. A homogeneous magnetic field will be applied either in axial $\mathbf{H} = H_z \mathbf{e}_z$ or in transverse $\mathbf{H} = H_x \mathbf{e}_x$ direction, respectively, where H_z and H_x indicate the field strengths. The length and time scales of the system are set by the gap width $d = R_2 - R_1$ and the diffusion time d^2/ν, respectively. The pressure in the fluid is normalized by $\rho \nu^2/d^2$, and the magnetic field $\mathbf{H}$ and the magnetization $\mathbf{M}$ can be conveniently normalized by the quantity $\sqrt{\rho/\mu_0} \nu/d$, where μ_0 is the permeability of free

space. These considerations lead to the following set of non-dimensionalized hydrodynamical equations[13,16]

$$(\partial_t + \mathbf{u} \cdot \nabla)\mathbf{u} - \nabla^2\mathbf{u} + \nabla p = (\mathbf{M} \cdot \nabla)\mathbf{H}$$
$$+ \frac{1}{2}\nabla \times (\mathbf{M} \times \mathbf{H}), \quad (1)$$

$$\nabla \cdot \mathbf{u} = 0. \quad (2)$$

The boundary conditions are set as follows. The velocities at the stationary boundaries (i.e., lids) are zero. The velocity fields on the cylindrical surfaces are given by $\mathbf{u}(r_1, \theta, z) = (0, Re_1, 0)$ and $\mathbf{u}(r_2, \theta, z) = (0, Re_2, 0)$, where the inner and outer Reynolds numbers are $Re_1 = \omega_1 r_1 d/\nu$ (fixed at 247 in the present study) and $Re_2 = \omega_2 r_2 d/\nu$ (fixed at 110 in the present study), respectively, where $r_1 = R_1/(R_2 - R_1)$ and $r_2 = R_2/(R_2 - R_1)$ are the non-dimensionalized inner and outer cylinder radii, respectively.

A. Ferrohydrodynamical equations

Equation (2) is to be solved together with an equation that describes the magnetization of the ferrofluid. Using the equilibrium magnetization of an unperturbed state in which the homogeneously magnetized ferrofluid is at rest and the mean magnetic moment is orientated in the direction of the magnetic field, we have $\mathbf{M}^{\mathrm{eq}} = \chi\mathbf{H}$. The magnetic susceptibility χ of the ferrofluid can be approximated by Langevin's formula,[42] where we set the initial value of χ to be 0.9 and use a linear magnetization law. The ferrofluid studied corresponds to APG933.[43] We consider the near equilibrium approximations of Niklas[10,44] with a small value of $\|\mathbf{M} - \mathbf{M}^{\mathrm{eq}}\|$ and small magnetic relaxation time $\tau : |\nabla \times \mathbf{u}|\tau \ll 1$. Based on these approximations, one can obtain the following magnetization equation:[13]

$$\mathbf{M} - \mathbf{M}^{\mathrm{eq}} = c_N^2\left(\frac{1}{2}\nabla \times \mathbf{u} \times \mathbf{H} + \lambda_2\mathbb{S}\mathbf{H}\right), \quad (3)$$

where

$$c_N^2 = \tau / \left(1/\chi + \tau\mu_0 H^2/6\mu\Phi\right), \quad (4)$$

is the Niklas coefficient,[10] μ is the dynamic viscosity, Φ is the volume fraction of the magnetic material, $\mathbb{S}$ is the symmetric component of the velocity gradient tensor,[13,16] and λ_2 is the material-dependent transport coefficient[16] that can be conveniently chosen to be $\lambda_2 = 4/5$.[11,16,45] Using Eq. (3), we can eliminate the magnetization from Eq. (2) to arrive at the following ferrohydrodynamical equations:[13,16]

$$(\partial_t + \mathbf{u} \cdot \nabla)\mathbf{u} - \nabla^2\mathbf{u} + \nabla p_M$$
$$= -\frac{s_N^2}{2}\left[\mathbf{H}\nabla \cdot \left(\mathbf{F} + \frac{4}{5}\mathbb{S}\mathbf{H}\right) + \mathbf{H} \times \nabla \times \left(\mathbf{F} + \frac{4}{5}\mathbb{S}\mathbf{H}\right)\right], \quad (5)$$

where $\mathbf{F} = (\nabla \times \mathbf{u}/2) \times \mathbf{H}$, p_M is the dynamic pressure incorporating all magnetic terms that can be expressed as gradients, and s_N is the Niklas parameter [Eq. (7)]. To the leading order, the internal magnetic field in the ferrofluid can be approximated by the externally imposed field,[41] which is reasonable for obtaining the dynamical solutions of the

magnetically driven fluid motion. Equation (5) can then be simplified as

$$(\partial_t + \mathbf{u} \cdot \nabla)\mathbf{u} - \nabla^2\mathbf{u} + \nabla p_M$$
$$= s_N^2\left\{\nabla^2\mathbf{u} - \frac{4}{5}[\nabla \cdot (\mathbb{S}\mathbf{H})] - \mathbf{H} \times \left[\frac{1}{2}\nabla \times (\nabla \times \mathbf{u} \times \mathbf{H})\right.\right.$$
$$\left.\left. - \mathbf{H} \times (\nabla^2\mathbf{u}) + \frac{4}{5}\nabla \times (\mathbb{S}\mathbf{H})\right]\right\}. \quad (6)$$

In this way, the effect of the magnetic field and the magnetic properties of the ferrofluid on the velocity field can be characterized by a single parameter, the magnetic field, or the Niklas parameter s_N.[10] A transverse (s_x) and a axial (s_z) magnetic fields can be described in more detail

$$s_x^2 = \frac{2(2 + \chi)H_x c_N}{(2 + \chi)^2 - \chi^2\eta^2}, \quad s_z^2 = H_z c_N, \quad (7)$$

where $0 \leq s_x, s_z \leq 1$.

B. Numerical methods

The ferrohydrodynamical equations of motion Eq. (5) can be solved by combining a standard, second-order finite-difference scheme in (r, z) with a Fourier spectral decomposition in θ and (explicit) time splitting.[11,13,41] The variables can be expressed as

$$f(r, \theta, z, t) = \sum_{m=-m_{\max}}^{m_{\max}} f_m(r, z, t) e^{im\theta}, \quad (8)$$

where f denotes one of the variables $\{u, v, w, p\}$. For the parameter regimes considered, the choice $m_{\max} = 10$ provides adequate accuracy. We use a uniform grid with spacing $\delta r = \delta z = 0.02$ and time steps $\delta t < 1/3800$.

Note that for a ferrofluid under a *transverse* magnetic field ($s_x \neq 0$), the symmetries presented in classical TCS confined by end walls (arbitrary rotations about the axis and the reflections about axial mid-height) are broken, and the flow is inherently three-dimensional for any non-zero values of the parameters Re_1, Re_2, and s_x.[11–13,41]

III. RESULTS

A. Multiple initial states

In the absence of any magnetic field, we find multi-stable flow states constituted by a combination of two local states: (1) locally spiral-shape structures (SPI$_l$) in the top and bottom of the annulus near the lids and (2) multi-cell flow states with toroidally closed vortices very close to the inner cylinder in the interior of the bulk. Note that these flow states depend on initial conditions. Specially, for these multi-cell states, we discovered flow states having *two* or *three* vortex cells (one vortex cell corresponds to one pair of counter-rotating Taylor-vortex structure), which are denoted by SPI$_{2V}$ and SPI$_{3V}$, respectively. Note that for larger aspect ratios (or longer cylinders), similar states with more such vortices can be existed.[36]

Visualizations of flow states combined by locally spiral-shape structures, SPI_l, and the multi-cell flow states, SPI_{3V} and SPI_{2V}, are illustrated in Figs. 1 and 2, respectively. Both flow states exhibit strongly pronounced and localized SPI_l structures in top and bottom of the annulus located near the lids. When compared with two initial flow states shown in Figs. 1(a) and 2(a), the locally spiral structure, SPI_l, shown in Fig. 1(a) is more strongly compressed due to the larger number of vortex pairs. It means that the helicity of SPI_{2V} in the spiral structures is larger than that of SPI_{3V}. From vector plots $[u(r, z), w(r, z)]$ shown in Figs. 2(b) and 1(b), we clearly see that the toroidally closed vortices are located very close towards the inner cylinder, which makes an almost *free* outer region in the center of the annulus, and SPI_{3V}'s central region in which the toroidally vortices within the multi-cell flow states are located is larger than that of SPI_{2V}. It produces slightly more compressed and localized spiral states in upper and lower part of the bulk near the lids.

Up to now, we found the flow states constituted by a combination of local flow states. To easily represent our flow states, we denoted them by following way:

- SPI_l: the flow has locally spiral shape structures at top and bottom lids (see Figs. 5 and 6).
- $SPI_{l+2V} = SPI_l + SPI_{2V}$: the flow has locally spiral shape structures at top and bottom lids and two-cell flow state with toroidally closed vortices at the interior of the bulk (see Fig. 2).
- $SPI_{l+3V} = SPI_l + SPI_{3V}$: the flow has locally spiral shape structures at top and bottom lids and three-cell flow state
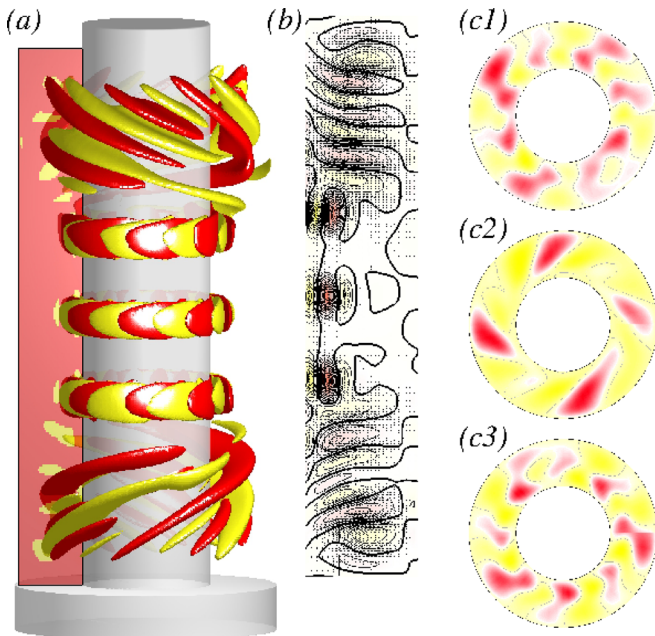

FIG. 1. Flow visualization of SPI_{l+3v}. Flow visualization of $SPI_l + SPI_{3V}$ for $s_x = 0$ and $s_z = 0$. (a) Isosurface of the azimuthal vorticity $\eta = (\nabla \times \mathbf{u})_\theta = \partial_z u - \partial_r w$ with isolevel $\eta = \pm 100$. (b) The corresponding vector plots $[u(r, z), w(r, z)]$ of the radial and axial velocity components [including azimuthal vorticity $\eta(r, \theta)$] at $\theta = 0$. (c1)–(c3) Azimuthal velocities $v(r, \theta)$ in three different planes at $z = 9\Gamma/10$, $\Gamma/2$, and $\Gamma/10$, respectively. Red (yellow) [dark (light gray)] contours correspond to positive [(negative)] values. Same visualizations are chosen for all unsteady, time dependent flow states in this paper.
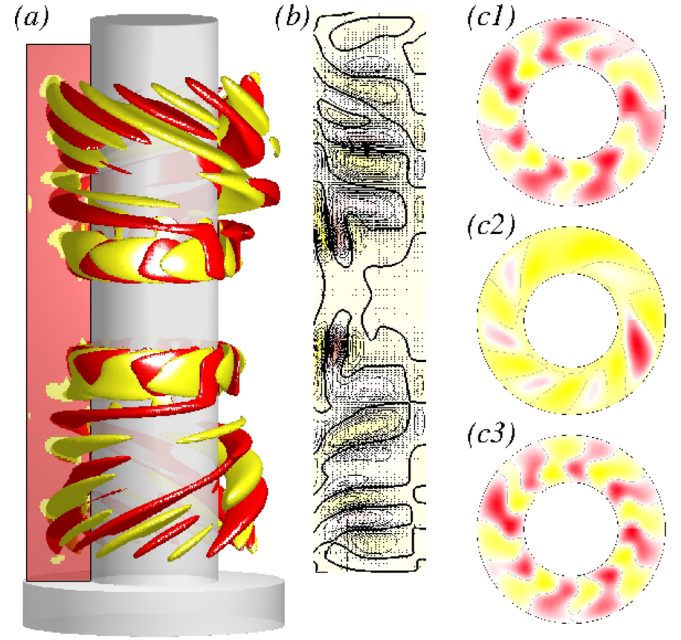

FIG. 2. Flow visualization of SPI_{l+2v}. Flow visualization of $SPI_l + SPI_{2V}$ for $s_x = 0$ and $s_z = 0$. The same visualizations as in Fig. 1 are shown. The isolevel at $\eta = \pm 90$ is shown in (a).

with toroidally closed vortices at the interior of the bulk (see Fig. 1).

In absence of any magnetic field, we find that the azimuthal mode amplitude $m = 8$ is to be preferred/predominant for the localized spirals in the bulk under the size and parameters of the considered system [see the cross-sections in (r, θ) plane of Figs. 1(c) and 2(c)]. However, in the center of the bulk within the small vortices, $m = 8$ does not play a significant role. Here, we find variations in lower azimuthal modes.

As a global measure characterizing the flow, we use the modal kinetic energy E_{kin}

$$E_{kin} = \sum_m E_m = \int_0^{2\pi} \int_{-\Gamma/2}^{\Gamma/2} \int_{r_i}^{r_o} \mathbf{u}_m \mathbf{u}_m^* r \, dr dz d\theta, \qquad (9)$$

where $\mathbf{u}_m$ ($\mathbf{u}_m^*$) indicates the m-th (complex conjugate) Fourier mode of the velocity field. Since E_{kin} is constant (non-constant) for a steady (an unsteady) solution, we consider the time-averaged quantity (over one period) for a diagnostic purpose

$$\bar{E}_{kin} = \int_0^T E_{kin} dt.$$

By varying two magnetic field strength s_x and s_z, respectively, we show the bifurcation scenarios for two initial flow states shown in Figs. 1 and 2, specially related to the modal kinetic energy E_{kin} [Fig. 3(1)] and the most energetic and dominant (averaged) mode amplitudes $|\bar{u}_{m,k}|$ [denoted as (m, k)] of the radial velocity at mid-gap and mid-height [Fig. 3(2)].

B. Effect of the axial magnetic field s_z

In the absence of any magnetic field, two initial flow states, SPI_{l+2v} and SPI_{l+3v}, are coexisting as multi-stable states. By
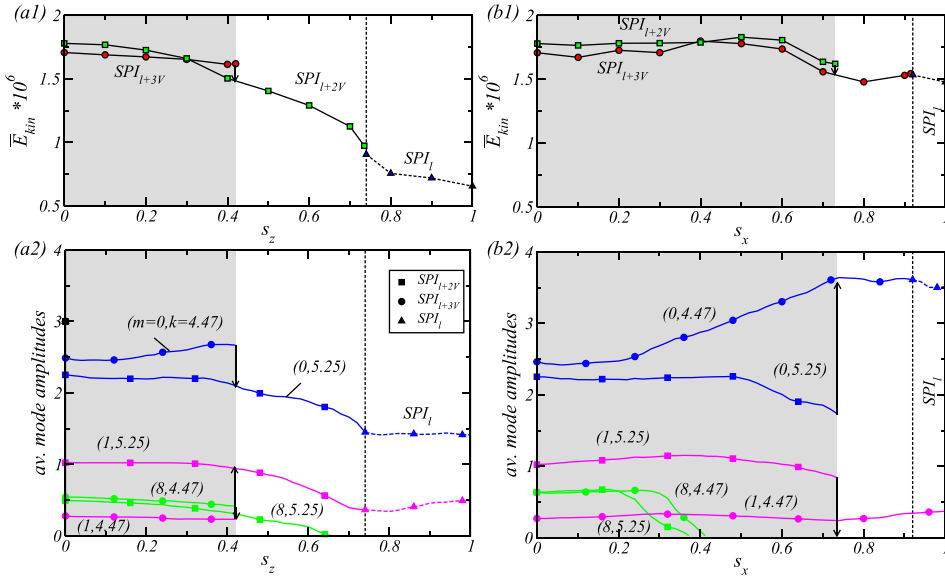
FIG. 3. Bifurcation scenarios. Bifurcation scenarios with (a) the time-averaged modal kinetic energy $\bar{E}_{kin}$ and (b) the dominant (averaged) amplitudes (m, k) of the radial velocity field at mid-gap contributed from the modes $m = 0$, 1, 8, respectively, for the axial (s_z-left column) and the transverse (s_x-right column) magnetic field strengths. Here, and in all the following figures, the gray colored region highlights the coexisting region of both flow states, SPI_{l+2V} and SPI_{l+3V}.

increasing the axial magnetic field strength s_z from zero, we will investigate dynamical changes in these two flow states.

Figure 3(a1) shows that for small $0 < s_z \lesssim 0.29$, the kinetic energy $\bar{E}_{kin}$ of SPI_{l+3V} is slightly smaller than that of SPI_{l+2V}, but for $0.29 \lesssim s_z \lesssim 0.43$, the kinetic energies $\bar{E}_{kin}$ of these two flow states is reversed, that is, the kinetic energy of SPI_{l+3V} is greater than that of SPI_{l+2V}. When $s_z \approx 0.43$, the flow state SPI_{l+3V} loses its stability and then becomes a *transient* toward the only stable solution branch with flow state SPI_{l+2V}, which is indicated by vertical arrows in Fig. 3, that is, $SPI_{l+3V} \rightarrow SPI_{l+2V}$. The flow state SPI_{l+2V} will exist before $s_z \lesssim 0.73$. When applied more strength of the axial magnetic field ($s_z \gtrsim 0.73$), we find that there is the second transient behavior going to *pure* SPI_l state ($SPI_{l+2V} \rightarrow SPI_l$) when the toroidally closed vortices disappear. However, $\bar{E}_{kin}$ continuously decrease with s_z, independent of two flow states. That is, by increasing the axial magnetic field strength, we find two time transient behaviors starting multi-stable states:

$$SPI_{l+2v}, SPI_{l+3v} \rightarrow SPI_{l+2v} \rightarrow SPI_l.$$

Figure 3(a2) presents the corresponding variations of the dominant (averaged) mode amplitudes (m, k). To make it, we use the azimuthal decomposition of the radial velocity field [see Eq. (8)]. From an axial Fourier analysis of the mode amplitudes $u_m(z, t)$ at mid-gap, $r = R_1 + d/2$, we identified the largest contribution in the axial Fourier spectrum of $u_m(z, t)$ for different m, which $k = 4.47$ for SPI_{l+3V} and $k = 5.24$ for SPI_{l+2V}. The moduli of these dominant Fourier amplitudes are denoted by (m, k), and its mode amplitudes are plotted in Fig. 3(a2) for the variation of s_z. Note that the axial wavenumber k is *not* constant and changes with s_x and s_z, respectively (see Fig. 4). As all flows are inherently 3D, for both flow states, SPI_{l+3V} and SPI_{l+2V}, multiple azimuthal modes m are finite. Aside the dominant axisymmetric $m = 0$ mode, Fig. 3(a2) also shows amplitudes of two more additional (non-axisymmetric) modes $m = 1$ and 8. We find that (1) these modes are most representative for two flow states and (2) the transient behavior between flow states can be existed in each representative mode. For instance, the flow

state SPI_{l+2V} has a significant pronounced $m = 1$ mode. On the other hand, $m = 8$ becomes eliminated by increasing s_z (i.e., the largest stimulated m becomes reduced and see also the cross-section (r, θ) plots in Fig. 5). Note that in principle, all modes are finitely stimulated but have all (minor) amplitudes. We found that the $m = 1$ mode is the only mode showing a significant jump/change during the transition behavior between two flow states, SPI_{l+2V} and SPI_{l+3V}, but all the other modes remain more or less the same (similar amplitude). Therefore, we may consider the visualization of $m = 1$.

Figure 5 elucidates selected flow states during the variation with s_z (see also Fig. 3). Topologically speaking, the
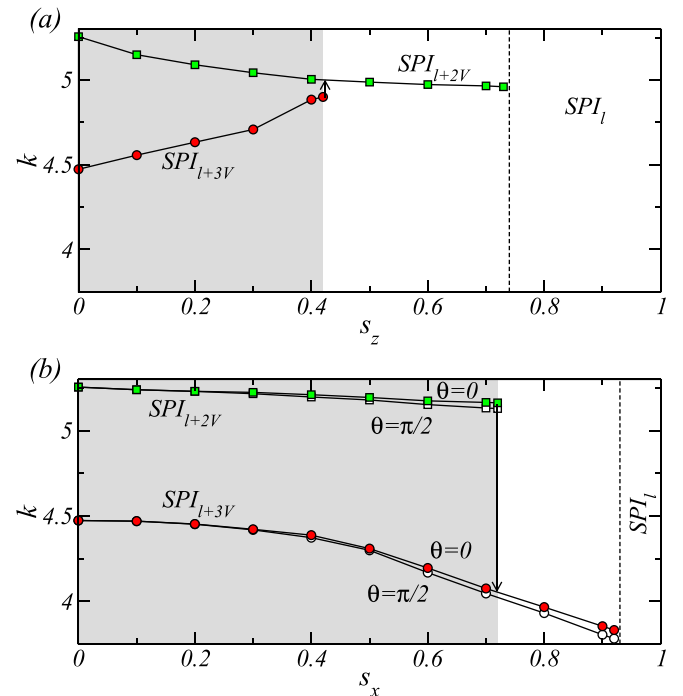

FIG. 4. Variation of the axial wavenumber k vs. magnetic field strength (s_z and s_x). Note that for $s_x \neq 0$ (b), the axial wavenumber in the directions along ($\theta = 0$) and perpendicular to ($\theta = \pi/2$) the magnetic field are slightly different[13,22] (see also Fig. 8).
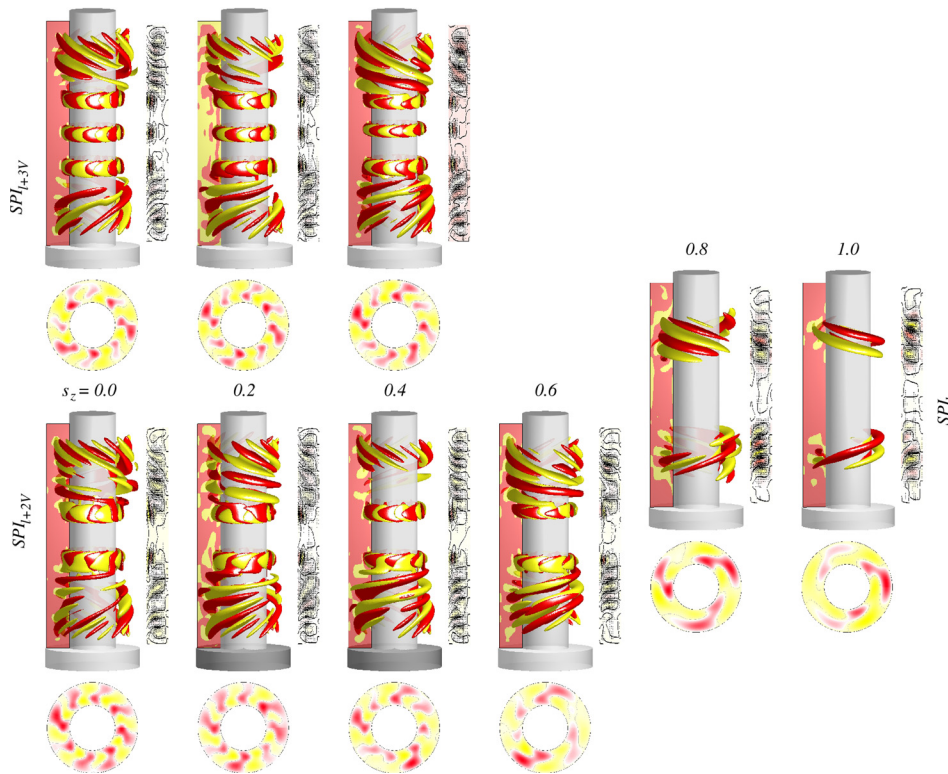
FIG. 5. Flow structures for various s_z. From top to bottom, flow structures of SPI_{l+3V}, SPI_{l+2V}, and SPI_l are shown by increasing the strength s_z of axial magnetic field. Isolevels of SPI_{l+3V}, SPI_{l+2V}, and SPI_l are $\eta = \pm 80$, $\eta = \pm 90$ and $\eta = \pm 50$, respectively. Right-hand side of and below each iso-surface plot, the corresponding vector plots $[u(r, z), w(r, z)]$ of the radial and axial velocity components at $\theta = 0$ [including azimuthal vorticity $\eta(r, \theta)$] and the cross-section plot of the azimuthal velocity $v(r, \theta)$ at $z = 0.1\Gamma$, respectively, are shown. Red (yellow) [dark (light gray)] contours correspond to the positive (negative) values.

flow structures of both SPI_{l+2V} and SPI_{l+3V} with different number of vortices are quite similar. In particular, small toroidally closed vortices of SPI_{l+3V} and SPI_{l+2V} locate more or less at their axial position. However, the dominant mode contribution within the localized spirals of SPI_{l+3V} and SPI_{l+2V} continuously decreases from initially $m = 8$ to $m = 3$ ($s_z \gtrsim 0.8$). For instance, the dominant mode of SPI_{l+2V} at $s_z = 0.6$ is $m = 6$ [see cross-section (r, θ) plots of

Fig. 5]. The reduction in the dominant azimuthal modes within the localized SPI can be also seen from the isosurfaces of vorticity, which clearly shows a decrease in slope when s_z is increasing.

When $s_z = 0.8$, we may observe that small toroidally vortices in the bulk disappear and SPI_l moves away from the lids towards the center of the bulk, as shown in Fig. 5. We may consider the movement of SPI_l state will be caused by
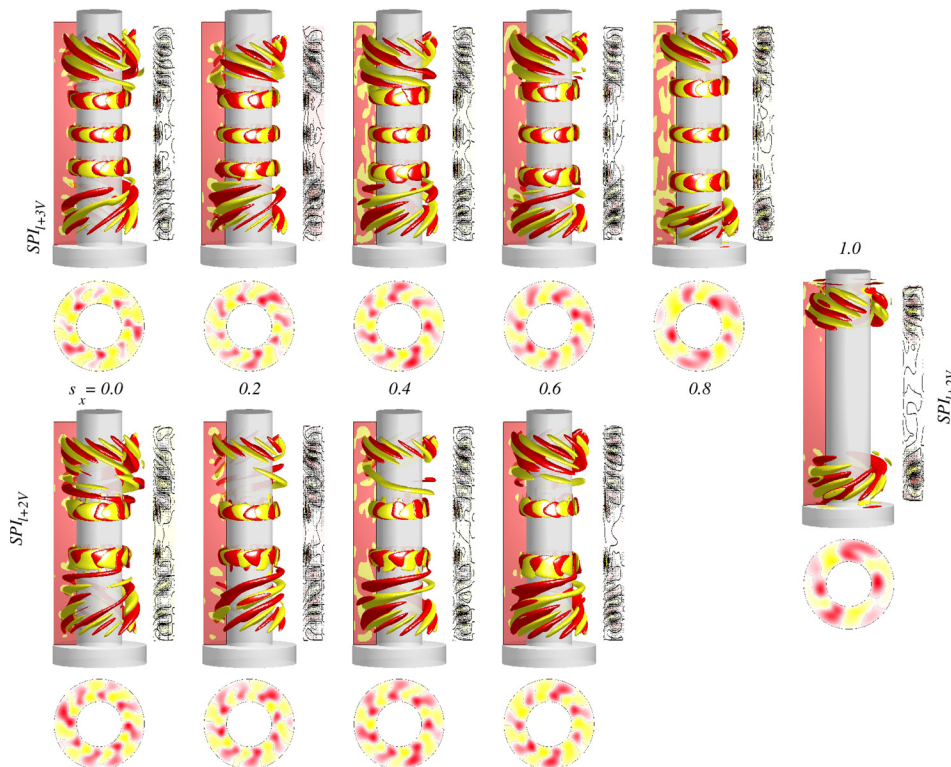

FIG. 6. Flow structures for various s_x. The same visualizations as in Fig. 5 are shown. Isolevels for SPI_{l+3V}, SPI_{l+2V}, and SPI_l are $\eta = \pm 80$, $\eta = \pm 90$, and $\eta = \pm 50$, respectively.
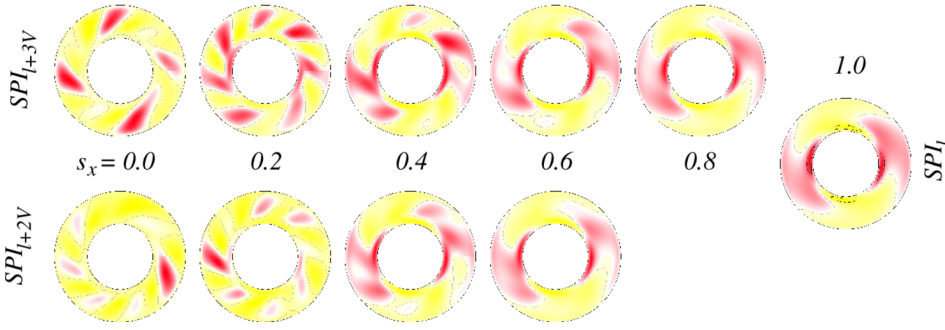
FIG. 7. Cross-section plots of SPI_{l+2V} and SPI_{l+3V} for various s_x. For each isosurface shown in Fig. 6, cross-section plots of the azimuthal velocity $v(r,\ \theta)$ at mid-height $z = \Gamma/2$ are shown. Red (yellow) [dark (light gray)] contours correspond to the positive (negative) values.

the *free* space created by the vanishing of small vortices. From the isosurface plots for SPI_{l+2V} at $s_z = 0.6$, we also see a slight moving of the SPI_l from the lids towards the interior of the bulk. Actually, this movement continuously happens until s_z is increasing about to 0.73, At $s_z \approx 0.73$, the toroidal vortices disappear. Therefore, we may find the transient behavior from SPI_{l+2V} to a pure SPI_l state.

C. Effect of a transverse magnetic field s_x

By increasing a strength s_x of a transverse magnetic field, we may observe a final flow state shown in Fig. 6, which could be compared to the bifurcation shown in Fig. 3(b1). The interesting thing is that a region of small vortices or a distance between vortices in the center of the annulus is continuously expanding along axial direction, which is satisfied for even both flow states SPI_{l+2V} and SPI_{l+3V}. In fact, the size of each vortex cell, that is, a pair of vortices, remains the same. That is, the distance between vortex centers is increasing with s_x. It induces that the localized spiral region near top and bottom lids is reduced by the extension of the vortices region. But, for large s_x, the small vortices disappear, and then, two flow states SPI_{l+2V} and SPI_{l+3V} are transient to SPI_l state. This transient phenomenon is observed when the axial magnetic field is applied. More detail, when $s_x \approx 0.73$, we find the first transient behavior from SPI_{l+2V} to SPI_{l+3V} and then the second transient from SPI_{l+3V} to SPI_l at $s_x \approx 0.92$

$$SPI_{l+2v},\ SPI_{l+3v} \rightarrow SPI_{l+3v} \rightarrow SPI_l.$$

With the increase in s_x, we observe the decrease in the dominant azimuthal mode m within the localized spirals, which could be seen from the cross-section plots $\eta(r,\ \theta)$ in Fig. 6. For instance, the dominant azimuthal mode for SPI_{l+2V} and SPI_{l+3V} is $m = 8$ at $s_x = 0.0$, 0.2, and $m = 7$ at $s_x = 0.4$, 0.6. But, at $s_x = 1.0$, the dominant modes of SPI_{l+3V} and SPI_{l+2V} are $m = 5$ and $m = 4$, respectively. From Sec. III B, we may conclude that the dominant azimuthal mode is decreased if the strength of a transverse or axial magnetic field is increasing.

Note that a transverse magnetic field tends to stimulate two-cell mode.[12,37,41] However, for studied parameters, this additional effect on $m = 2$ is relatively small compared with all other stimulated modes. It only becomes visible in the central region of the bulk for sufficient large value s_x. By increasing s_x, Fig. 7 shows cross-sections at mid-height, which illustrate the dominance of the $m = 2$ mode. For $s_x \gtrsim 0.4$, the dominance of the $m = 2$ mode is evident either

for SPI_{l+2V} or for SPI_{l+3V} and most pronounced in SPI_l after all inner bulk vortices disappeared.

From a comparison between the location of local SPI_l states shown in Figs. 5 and 6, we clearly distinguish two SPI_l states generated by different magnetic fields. That is, by increasing axial magnetic field s_x, the local SPI_l moves from the Ekman region near the lids towards the interior of the bulk (Fig. 5), but the SPI_l becomes pushed into the Ekman vortex region by increasing a transversal magnetic field (see Fig. 6, i.e., best visible in vector plots $[u(r, z), w(r, z)]$). After two flow states, SPI_{l+3V} and SPI_{l+2V}, are transient to the pure SPI_l by different magnetic fields, we clearly observe the different positions of SPI_l. That is, different magnetic fields induce the different movements of SPI_l, here in the opposite direction.

From releasing the space of the small vortices after the elimination of the 3-cell state, it might be expected that the localized SPI_l will penetrate further into the bulk. But this is not the case that the main/central region of the annulus remains without any significant flow structure {see vector plots $[u(r, z), w(r, z)]$ in Fig. 6 at $s_x = 1.0$}.

D. Variation of wavenumber k

As mentioned in the previous Secs. III B and III C there is a change in the axial wavenumber k by increasing a strength of both magnetic fields. In particular, when a region of the small vortices in the bulk is enlarged (see Fig. 6), a change in wavenumber k is stronger, as shown in Fig. 4. Even when the wavenumber for SPI_{l+2V} monotonously decreases for both magnetic fields, SPI_{l+3V}'s wavenumber is monotonically increasing (decreasing) for the axial (transverse) magnetic field. To discuss in more detail, when increasing s_z, the wavenumber of SPI_{l+3V} is continuously increasing towards SPI_{l+2V}'s wavenumber before losing its stability, but it never reaches/touches them. In contrast, with increasing s_x, the wavenumber for SPI_{3V} is continuously decreasing. It means that due to the symmetry breaking effect of a transverse magnetic field, the changes in wavenumbers in the direction along parallel ($\theta = 0$) and perpendicular ($\theta = \pi/2$) to the magnetic field are induced.[11–13,22]

Figure 8 shows profiles of the axial velocity w, which illustrates a change in wavenumber k and wavelength $k/2\pi$ with increasing s_x or s_z. Comparing each SPI_l's profiles at $s_x = 1.0$ and $s_z = 1.0$, one can clearly see the different location of the localized spirals. That is, SPI_l with $s_x = 1.0$ stays close to the lids in the Ekman bound-layer region, but SPI_l
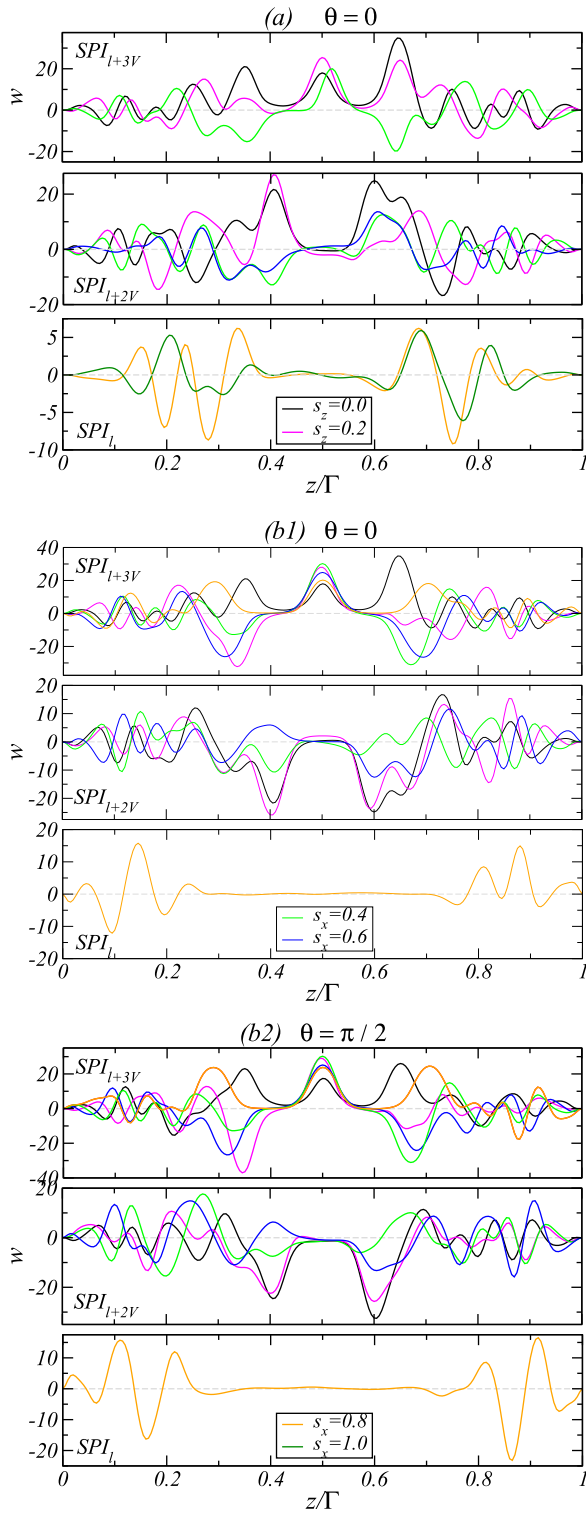
FIG. 8. Axial velocity profiles w for a magnetic field strength (s_z and s_x). Axial velocity profiles w in the annulus at the mid-gap location for different s_z (a) and s_x (b) are indicated. Note that for $s_x \neq 0$, the profiles w are different for $\theta = 0$ (b1) and $\theta = \pi/2$ (b2) in the annulus at the mid-gap location.[12,13,22] (See also Fig. 4).

with $s_z = 1.0$ is further away from the lids penetrating towards the interior of the annulus. Thus, for $s_x = 1.0$, there is a quite wide empty region, almost without any or at least very few dynamics in the center of the annulus, which can be seen from the flat profiles shown in Figs. 8(b1) and 8(b2).

E. Angular momentum and torque

To characterize dynamics of a ferrofluid system with influence of the axial and transverse magnetic fields, we examine an angular momentum and a torque for various flow structures. Figure 9(a) shows a mean angular momentum $L(r) = r\langle v(r)\rangle_{\theta,z}/Re_1$ which can be defined as a function of the radius r with axial and azimuthal average for each s_x and s_z. The interesting thing is that angular momentum curves $L(r)$ for each flow state show almost same shapes with slight variation in the slopes (gradients). In particular, the profiles $L(r)$ for SPI_{l+2V} and SPI_{l+3V} with the same magnitude s_z and s_x are almost indistinguishable. That is, they show virtually no differences. However, for increasing s_z, the profiles (mainly the central region; see the expanded view, the insets in Fig. 9) are decreasing, but they are increasing for s_x. The effect is strongest for pure SPI_l at large strength s_x and s_z, respectively. In general, the effect of s_z is weaker than for s_x at the same strength.

A dimensionless torque $G(r)$ within the annulus can be defined by $G(r) = \nu J^\omega$, where $J^\omega = r^3[\langle u\omega\rangle_{A,t} - \nu\langle\partial_r\omega\rangle_{A,t}]$ and $\langle\ldots\rangle_A \equiv \int\frac{rd\theta dz}{2\pi rl}$. To calculate the torque $G(r)$, we use the fact that for a flow between infinite cylinders, the transverse current of the azimuthal motion is conserved.[46] For different s_z, Fig. 9(b) shows the variations of the torque profiles, but its variations are too small. With increasing s_z, the torque profiles show almost same values at the central region, but their decrease can be observed in the outer region [see the inset of Fig. 9(b)]. There are only minimal differences for the torque profiles of SPI_{l+2V} and SPI_{l+3V} at same s_z, but at least visible. For a different s_x, the torque profiles for flow states show stronger changes. By increasing s_x, they decrease in the inner region, but are significant in the central and outer region. About the total torque G_{total} shown as in Fig. 9(c), it shows different behaviors with increasing s_z and s_x. That is, it decreases with s_z, but increases with s_x. We note that it is independent of the flow states, SPI_{l+2V}, SPI_{l+3V}, or SPI_l.

F. Transitions between SPI_{l+3V} and SPI_{l+2V}

As discussed before, by increasing s_x (s_z), SPI_{l+3V} (SPI_{l+2V}) loses its stability and then is transient towards SPI_{l+2V} (SPI_{l+3V}), respectively. Now, we investigate these transition behavior in more detail.

1. SPI_{l+3V} toward SPI_{l+2V}

When the strength s_z of the axial magnetic field is greater than the critical strength, that is, $s_z \gtrsim 0.43$, the transient behavior from SPI_{l+3V} to SPI_{l+2V} could be happened in a somehow expected manner. That is, after combining upper two vortex pairs of the initially three vortex pairs, it leaves only two vortex pairs behind. Note that the equal transition can be also happened combining the lower two vortex pairs. Both scenarios have been observed in simulations. A more detailed perspective of the evolution from SPI_{l+3V} to SPI_{l+2V} is available in the supplementary materials (See movieA1.avi and movieA2.avi).

During the transition from SPI_{l+3V} to SPI_{l+2V}, in order to observe the changes in some quantities in time, we
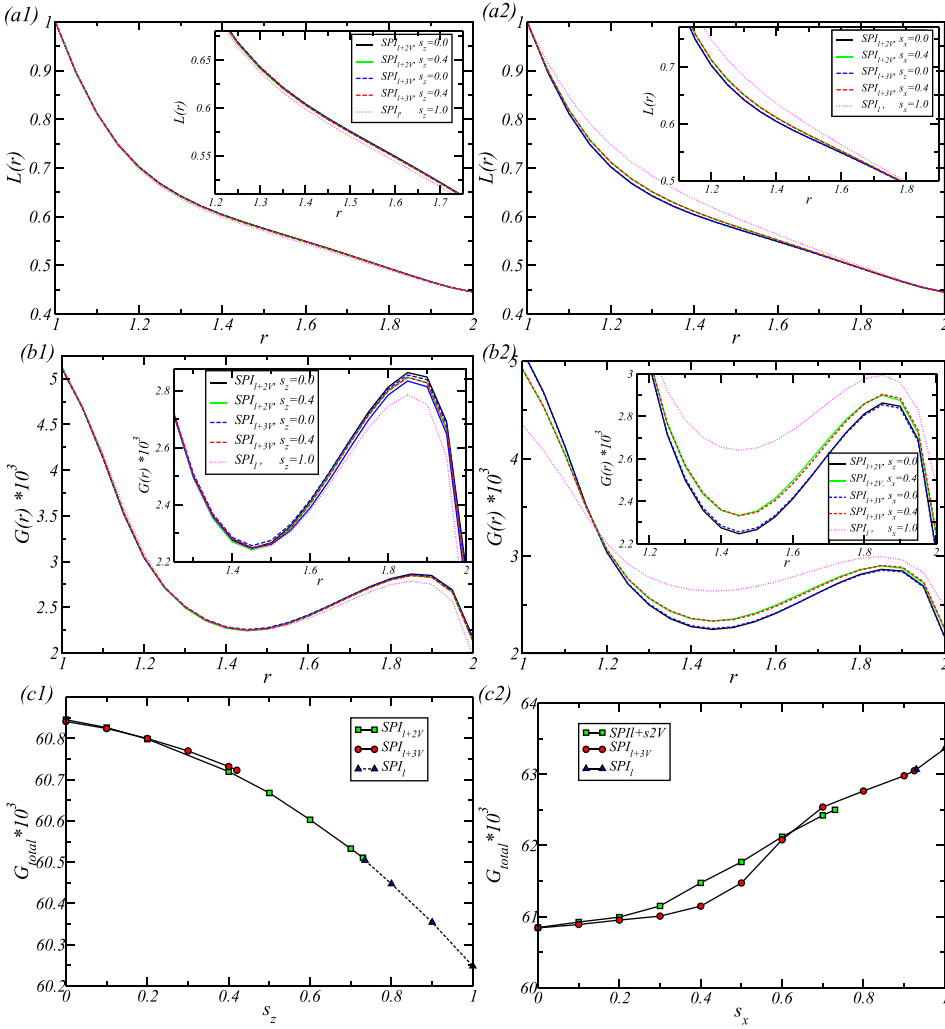
FIG. 9. Angular momentum $L(r)$ for SPI_{l+2V} and SPI_{l+3V}. (a) Angular momentum $L(r) = r\langle v(r)\rangle_{\theta,z}/Re_1$ scaled with the inner Reynolds number Re_1 versus the radius r for SPI_{l+2V}, SPI_{l+3V} and SPI_l with s_z (1) and s_x (2), respectively. (b) Variation of the dimensionless torque $G = \nu J^\omega$ (see text for details) versus the radius r. (c) Total torque G_{total} with s_z and s_x, respectively.

investigate time series of the modal kinetic energy $E_{kin}(t)$, a mode amplitude $|u_{m,k}|$ of the radial velocity field, and azimuthal vorticity. Typically, $E_{kin}(t)$ is fluctuating around $\bar{E}_{kin}$. To clearly observe a change in the modal kinetic energy, we also consider a sequence of an averaged modal kinetic energy over a fixed time T

$$E_{kin}(n, T) = \frac{1}{T}\int_{(n-1)T}^{nT} E_{kin}(t)dt \quad \text{for } n = 0, 1, \ldots. \quad (10)$$

For different time-averaged modal kinetic energies $\bar{E}_{kin}$ for two flow states, that is, $\bar{E}_{kin}(SPI_{l+3v}) \neq \bar{E}_{kin}(SPI_{l+2v})$, a change in $E_{kin}(n)$ in time shows an energy transition from $\bar{E}_{kin}(SPI_{l+3v})$ to $\bar{E}_{kin}(SPI_{l+2v})$, as shown in Fig. 10(a). For a moment of a transition occurrence between two flow states, Figs. 10(a)–10(c) show the changes in a modal kinetic energy and the mode amplitude, and the space-time plot of the azimuthal vorticity. Due to a complex interaction between various non-linear terms, $E_{kin}(t)$ indicates quite strong time-dependent modulations as shown in Fig. 10(a). But it shows that $E_{kin}(t)$ is fluctuating around $\bar{E}_{kin}(SPI_{l+3v})$ before transition and then tends to jump down to the energy level of $\bar{E}_{kin}(SPI_{l+2v})$ in order to fluctuating around $\bar{E}_{kin}(SPI_{l+2v})$.

About the quantity of the mode amplitudes, Fig. 10(b) presents clear evidence for the change in the wavenumber, which is coincide with the decrease in three to two toroidally

closed vortices in the bulk, and the significant part of the transition process for $0.78 \lesssim t \lesssim 1.56$. Figure 10(c) shows the space-time plot of the azimuthal vorticity illustrating the merge of two vortices. After the two vortices merged into one vortex pair at $t \approx 1.3$, the remaining two vortices continuously exist in parallel.

Figure 11 presents the corresponding spatio-temporal vortex structures by isosurfaces of the azimuthal vorticity at time t marked by the small arrows shown in Figs. 10(b) and 10(c). The first two figures of Fig. 11 present a movement of the central vortex pair to upwards the upper vortex pair. After the movement, there is a strong compression of the upper vortex pair in size, and then, two vortex pairs are merged [See Figs. 11(3) and 11(4)]. Finally, a SPI_{l+2V} state remains continuously in the annulus, which can be compared to the change in the modal kinetic energy $E_{kin}(t)$ shown in Fig. 10(a).

2. SPI_{l+2V} to SPI_{l+3V}

The transient process from SPI_{l+3V} to SPI_{l+2V} is not followed by an intuitive expectation, that is, just creating an additional vortex pair (See also movieB1.avi and movieB2.avi in supplementary materials). After SPI_{l+2V} loses its stability, the flow state will stay an intermediately *pure* SPI state (SPI_l) without having any toroidally closed vortices in the bulk
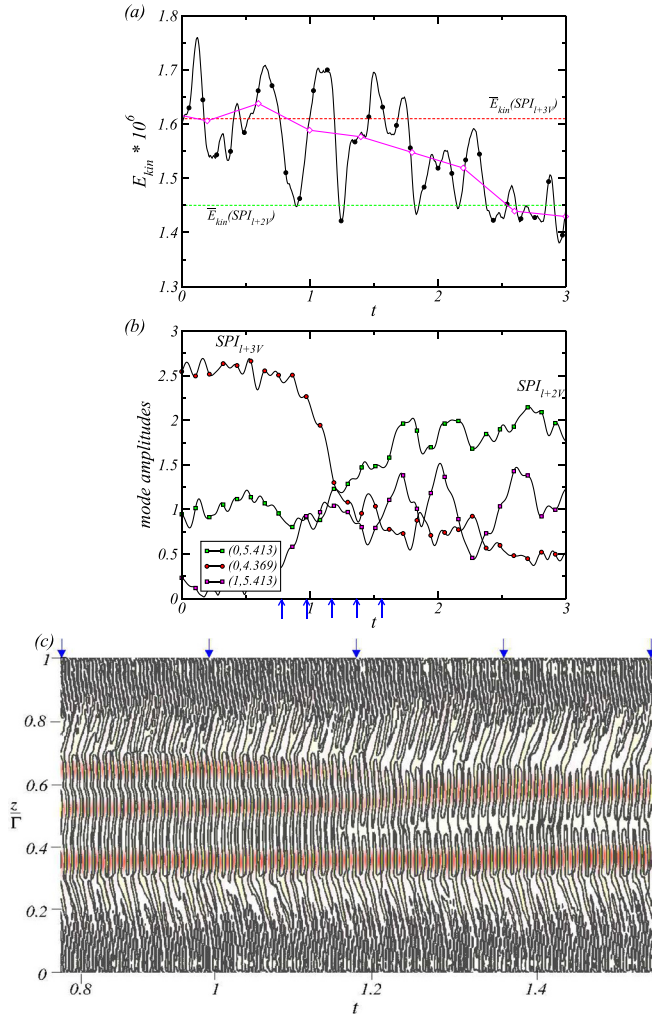
FIG. 10. Transitions from SPI_{l+3V} to SPI_{l+2V}. (a) Time evolution of modal kinetic energy E_{kin} and $E_{kin}(n, T)$, and (b) selected dominant amplitudes $|u_{m,k}|$ of the radial velocity field at mid-gap contributed from the axisymmetric modes $m = 0$ and the non-axisymmetric $m = 1$ mode, respectively. Corresponding axial wavenumbers k as indicated. The dashed lines present the long-time averaged energies E_{kin} of flows as indicated (see also Fig. 3). (c) Corresponding space-time plot of the azimuthal vorticity η during the transition at $r = r_1 + 0.1d$. Red (dark gray) and yellow (light gray) correspond to positive and negative values, with $\eta \in [-440, 440]$. The short blue arrows below (above) the abscissa in (b) [(c)] identify the time-values of the snapshots in Fig. 10(b). We have chosen $T = 4$ for $E_{kin}(n)$ [see Eq. (10)], resulting in best visualization for transition.

(for $0.5 \lesssim t \lesssim 0.8$ in Fig. 12). To create a final state SPI_{l+3V}, two vortices are first generated from the scratch, and then, an additional vortex pair is created in the center of the bulk. That is, in very short time, the transient process is happened in following way:

$$SPI_{l+2v} \rightarrow SPI_l \rightarrow SPI_{l+2v} \rightarrow SPI_{l+3v}.$$

Figure 12 shows the changes in quantities during the transient process. The modal kinetic energy $E_{kin}(t)$ is fluctuating in the short transient time, but moves to the energy level, $\bar{E}_{kin}(SPI_{l+3v})$, and then fluctuates around it. It means that before and after a transient process, we may observe a transition of the modal kinetic energy [See Fig. 12(a)]. During a transition toward SPI_{l+3V}, more changes in the dominant mode amplitude of SPI_{l+3V} can be observed.
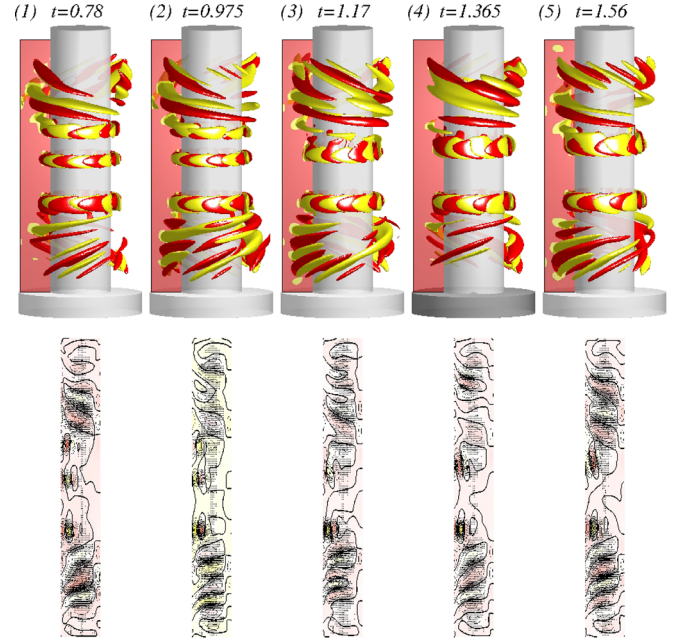

FIG. 11. Vortex structures during the transitions from SPI_{l+3V} to SPI_{l+2V}. Spatio-temporal changes of the vortex structure in the transition $SPI_{l+3V} \rightarrow SPI_{l+2V}$ (from left to right). See also movieA1.avi and movieA2.avi in supplementary materials. Time for the five snapshots is marked by arrows at the abscissas of Figs. 10(b) and 10(c).

Figure 12(b) shows this change or an increase in the dominant mode amplitude at the time $0.5 \lesssim t \lesssim 1.2$. The dominant mode amplitude for SPI_{l+2V} is decreasing and vanishing at $t \approx 0.7$, which is corresponding to the disappearance of SPI_{l+2V}. To generate a new SPI_{l+2V} in the transient process, the dominant mode amplitude is starting to increase until $t \gtrsim 0.95$. After creating the center vortex pair, it is decreasing, which can be corresponding to the formation of SPI_{l+3V}. The space-time plot of the azimuthal vorticity shown in Fig. 12(c) illustrates a temporal elimination of all toroidally closed vortices, the state SPI_l, the generation of SPI_{l+2V}, and the final state SPI_{l+3V} in time order. Figure 13 presents the corresponding spatio-temporal vortex structures by isosurfaces of the azimuthal vorticity at time t marked by the small arrows shown in Figs. 12(b) and 12(c). The first three figures of Fig. 13 show a disappearing process of all toroidally closed vortices, and for the last two figures of Fig. 13, a generating process of the SPI_{l+3V} state. Through performing various simulations, we always observed the same scenario eliminating the two central vortex pairs and regenerating the three vortex cell states. The latter happens in two steps: (1) Generating both outer cell states and then (2) the inner vortex cell. This principle lets us speculate that the SPI_l is a structure creating a global circulation.

IV. DISCUSSION AND CONCLUSION

As a foundational paradigm of fluid dynamics, the Taylor-Couette System has been extensively investigated computationally and experimentally. In spite of the long history of the TCS and the vast literature on the subject, recently the dynamics of TCS with a ferrofluid subject to a magnetic field has begun to be investigated relatively. In this
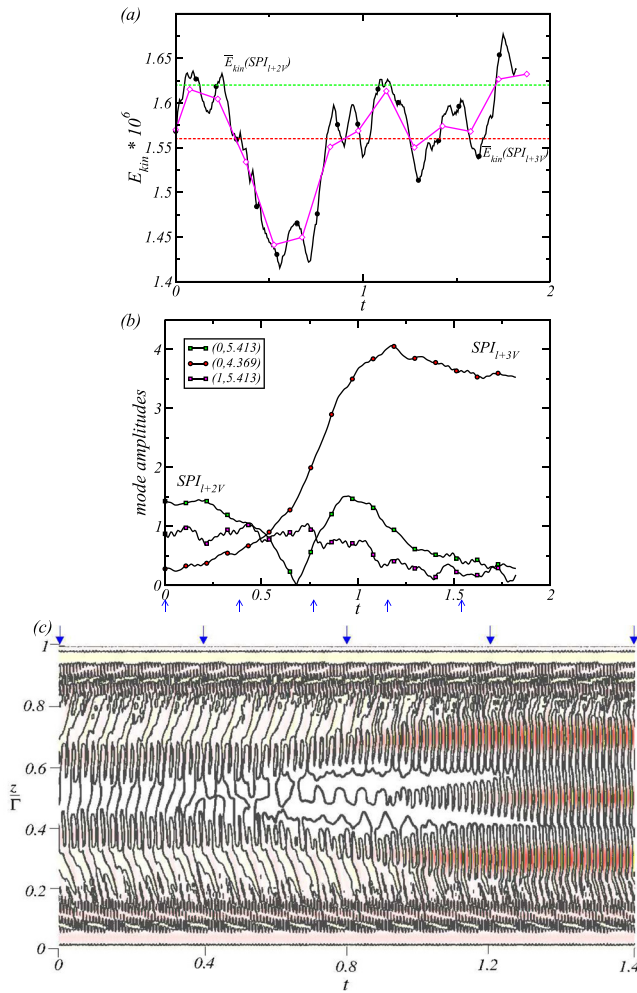
FIG. 12. Transitions from SPI_{l+2V} to SPI_{l+3V}. The same visualization as in Fig. 10 are shown but the transition behavior is from SPI_{l+2V} to SPI_{l+3V}. Red (dark gray) and yellow (light gray) correspond to positive and negative values, respectively, with $\eta \in [-332, 332]$. Here, we have chosen $T = 0.15$ for $E_{kin}(n, T)$.

FIG. 13. Vortex structures during the transition from SPI_{l+2V} to SPI_{l+3V}. Spatio-temporal changes of the vortex structure in the transition $SPI_{l+3V} \rightarrow SPI_{l+2V}$ (from left to right). See also movieB1.avi and movieB2.avi in supplementary materials. The time for the five snapshots is marked by arrows at the abscissas of Figs. 12(b) and 12(c).

paper, we study the ferrofluidic Taylor-Couette flow between co-rotating cylinders, enclosed by stationary disks, with focus on the global boundary-driven circulation under the influence of axial and transverse magnetic fields. Through systematic and extensive simulations of the ferrohydrodynamical equations, a generalization of the classic Navier-Stokes equation into ferrofluidic systems subject to a magnetic field, we study the emergence and evolution of distinct dynamical flow states.

Without applying any magnetic fields, we found the emergence of two flow states constituted by a combination of a localized spiral state (SPI_l) in the top and bottom of the annulus and different multi-cell flow states (SPI_{2v}, SPI_{3v}) with toroidally closed vortices in the interior of the bulk ($SPI_{l+2v} = SPI_l + SPI_{2v}$ and $SPI_{l+3v} = SPI_l + SPI_{3v}$). That is, we found multi-stable states, which are depending on initial conditions.

When applying magnetic fields, we found that the presence of magnetic fields can stipulate all flow states, leading to the transitions among various flow states, for example, the two-cell and three-cell flow states. The emergence of the flow states, dynamical evolution, and transitions among the various flow states can be summarized in detail, as follows. By increasing
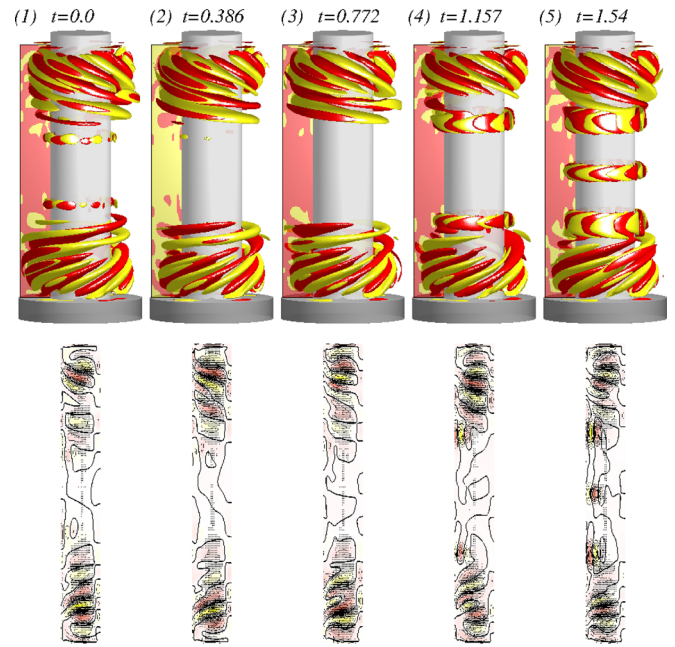
the axial (transverse) magnetic field strength, we first identify a transition from $SPI_{l+3v}(SPI_{l+2v})$ to $SPI_{l+2v}(SPI_{l+3v})$, respectively. However, for strong enough magnetic fields, we discover the second transition going to SPI_l state.

Although the flow states under fairly large magnetic fields (s_x or s_z) are SPI_l, there is a significant difference between two final SPI_l states. For applying the strong transverse magnetic field (s_x), SPI_l is oriented close to top and bottom lid located in the Ekman vortex regime. But SPI_l under the strong axial magnetic field (s_z) is oriented more towards the center of the bulk. According to the different type of magnetic fields, SPI_l state can move to or away from the Ekman region.

The transitions between the multi-cell flow states are always accompanied by a change in the wavelength and wavenumber, respectively. However, in the present study the symmetry breaking effect (a stimulated two-cell mode[12,37,41]) of the transverse magnetic field is obviously present, but plays a significant minor role than in other studies. It becomes more and more pronounced for the larger magnetic field strength s_x and s_z.

It may be challenging to detect transient behaviors experimentally as they coexist with other complex states such as SPI_{l+3v}, SPI_{l+2v} and SPI_l. We are hopeful that our finding will stimulate further research of controlling the ferrofluidic systems.

SUPPLEMENTARY MATERIAL

See supplementary materials for the complete spatio-temporal evolution between SPI_{l+2V} to SPI_{l+3V} or vice versa.

ACKNOWLEDGMENTS

[1] G. I. Taylor, "Stability of a viscous liquid contained between two rotating cylinders," Philos. Trans. R. Soc. London A **223**, 289 (1923).

[2] P. Chossat and G. Iooss, *The Couette–Taylor Problem* (Springer, Berlin, 1994).

[3] C. A. Jones, "The transition to wavy Taylor vortices," J. Fluid Mech. **157**, 135–162 (1985).

[4] R. C. DiPrima and H. L. Swinney, "Instabilities and transition in flow between concentric rotating cylinders," in *Hydrodynamic Instabilities and the Transition to Turbulence*, Topics in Applied Physics Vol. 45, edited by H. L. Swinney and J. G. Gollub (Springer, Berlin, 1985).

[5] C. D. Andereck, S. S. Liu, and H. L. Swinney, "Flow regimes in a circular Couette system with independently rotating cylinders," J. Fluid Mech. **164**, 155–183 (1986).

[6] M. Golubitsky and W. F. Langford, "Pattern formation and bistability in flow between counterrotating cylinders," Physica D **32**, 362–392 (1988).

[7] R. E. Rosensweig, *Ferrohydrodynamics* (Cambridge University Press, Cambridge, 1985).

[8] J. P. McTague, "Magnetoviscosity of magnetic colloids," J. Chem. Phys. **51**, 133 (1969).

[9] M. I. Shliomis, "Effective viscosity of magnetic suspensions," Sov. Phys. JETP **34**, 1291 (1972).

[10] M. Niklas, "Influence of magnetic fields on Taylor vortex formation in magnetic fluids," Z. Phys. B **68**, 493 (1987).

[11] S. Altmeyer, C. Hoffmann, A. Leschhorn, and M. Lücke, "Influence of homogeneous magnetic fields on the flow of a ferrofluid in the Taylor-Couette system," Phys. Rev. E **82**, 016321 (2010).

[12] M. Reindl and S. Odenbach, "Effect of axial and transverse magnetic fields on the flow behavior of ferrofluids featuring different levels of interparticle interaction," Phys. Fluids **23**, 093102 (2011).

[13] S. Altmeyer, J. Lopez, and Y. Do, "Effect of elongational flow on ferrofuids under a magnetic field," Phys. Rev. E **88**, 013003 (2013).

[14] O. Ambacher, S. Odenbach, and K. Stierstadt, "Rotational viscosity in ferrofluids," Z. Phys. B **86**, 29 (1992).

[15] S. Odenbach and H. Gilly, "Taylor-vortex flow of magnetic fluids under the influence of an azimuthal magnetic field," J. Magn. Magn. Mater. **152**, 123–128 (1996).

[16] H. W. Müller and M. Liu, "Structure of ferrofluid dynamics," Phys. Rev. E **64**, 061405 (2001).

[17] S. Odenbach, *Magnetoviscous Effects in Ferrofluids*, Lecture Notes in Physics Vol. m71 (Springer, Berlin, 2002).

[18] M. I. Shliomis, "'Comment on' structure of ferrofluid dynamics," Phys. Rev. E **67**, 43201 (2003).

[19] A. Leschhorn, M. Lücke, C. Hoffmann, and S. Altmeyer, "Stability of circular Couette flow of a ferrofluid in an axial magnetic field: Influence of polydispersity," Phys. Rev. E **79**, 036308 (2009).

[20] M. Reindl and S. Odenbach, "Influence of a homogeneous axial magnetic field on Taylor-Couette flow of ferrofluids with low particle-particle interaction," Exp. Fluids **50**, 375–384 (2011).

[21] S. Altmeyer, "Untersuchungen von komplexen Wirbelströmungen mit newtonschem fluid und Ferrofluiden im Taylor-Couette system," Doktorarbeit (Universität des Saarlandes, Saarbrücken, 2011).

[22] S. Altmeyer, Y.-H. Do, and Y.-C. Lai, "Transition to turbulence in Taylor-Couette ferrofluidic flow," Sci. Rep. **5**, 10781 (2015).

[23] S. Altmeyer, Y.-H. Do, and Y.-C. Lai, "Magnetic field induced flow reversal in a ferrofluidic Taylor-Couette system," Sci. Rep. **5**, 18589 (2015).

[24] J. E. Hart, "A magnetic fluid laboratory model of the global buoyancy and wind-driven ocean circulation: Analysis," Dyn. Atmos. Oceans **41**, 121–138 (2006).

[25] J. E. Hart and S. Kittelman, "A magnetic fluid laboratory model of the global buoyancy and wind-driven ocean circulation: Experiments," Dyn. Atmos. Oceans **41**, 139–147 (2006).

[26] M. C. Cross and P. C. Hohenberg, "Pattern formation outside of equilibrium," Rev. Mod. Phys. **65**(3), 851 (1993).

[27] M. Nagata, "On wavy instabilities of the Taylor-vortex flow between corotating cylinders," J. Fluid Mech. **188**, 585 (1988).

[28] R. Hollerbach and G. Rudiger, "New type of magnetorotational instability in cylindrical Taylor-Couette flow," Phys. Rev. Lett. **95**, 124501 (2005).

[29] F. Tefani *et al.*, "Experimental evidence for magnetorotational instability in a Taylor-Couette flow under the influence of a helical magnetic field," Phys. Rev. Lett. **97**, 184502 (2006).

[30] M. S. Paoletti and D. P. Lathrop, "Angular momentum transport in turbulent flow between independently rotating cylinders," Phys. Rev. Lett. **106**, 024501 (2011).

[31] D. P. M. van Gils, S. G. Huisman, G. W. Bruggert, C. Sun, and D. Lohse, "Torque scaling in turbulent Taylor-Couette flow with co- and counterrotating cylinders," Phys. Rev. Lett. **106**, 024502 (2011).

[32] M. Burin *et al.*, "Reduction of Ekman circulation within Taylor-Couette flow," Exp. Fluids **40**, 962–966 (2006).

[33] E. Schartman, H. Ji, and M. J. Burin, "Reduction of Ekman circulation within Taylor-Couette flow," Rev. Sci. Instrum. **80**, 024501 (2009).

[34] T. Benjamin, "Bifurcation phenomena in steady flows of a viscous fluid. I. theory," Philos. Trans. R. Soc. A **359**, 1–26 (1978).

[35] T. Benjamin, "Bifurcation phenomena in steady flows of a viscous fluid. II. experiments," Philos. Trans. R. Soc. A **359**, 27–43 (1978).

[36] M. Heise *et al.*, "Co-rotating Taylor-Couette flow enclosed by stationary disks," J. Fluid Mech. **716**, R4 (2013).

[37] S. Altmeyer *et al.*, "End wall effects on the transitions between Taylor vortices and spiral vortices," Phys. Rev. E **81**, 066313 (2010).

[38] M. Heise *et al.*, "Localized spirals in Taylor-Couette flow," Phys. Rev. E **77**, 026202 (2008).

[39] J. Abshagen, M. Heise, G. Pfister, and T. Mullin, "Multiple localized states in centrifugally stable rotating flow," Phys. Fluids **22**, 021702 (2010).

[40] C. Hoffmann, S. Altmeyer, M. Heise, J. Abshagen, and G. Pfister, "Axisymmetric propagating vortices in centrifugally stable Taylor-Couette flow," J. Fluid Mech. **728**, 458–470 (2013).

[41] S. Altmeyer, J. Lopez, and Y. Do, "Influence of an inhomogeneous internal magnetic field on the flow dynamics of ferrofluid between differentially rotating cylinders," Phys. Rev. E **85**, 066314 (2012).

[42] P. Langevin, "Magnétisme et théorie des électrons," Ann. Chem. Phys. **5**, 70–127 (1905).

[43] J. Embs, H. W. Müller, C. Wagner, K. Knorr, and M. Lücke, "Measuring the rotational viscosity of ferrofluids without shear flow," Phys. Rev. E **61**, R2196–R2199 (2000).

[44] M. Niklas, H. Müller-Krumbhaar, and M. Lücke, "Taylor–vortex flow of ferrofluids in the presence of general magnetic fields," J. Magn. Magn. Mater. **81**, 29 (1989).

[45] S. Odenbach and H. W. Müller, "Stationary off-equilibrium magnetization in ferrofluids under rotational and elongational flow," Phys. Rev. Lett. **89**, 037202 (2002).

[46] B. Eckhardt, S. Grossmann, and D. Lohse, "Torque scaling in turbulent Taylor-Couette flow between independently rotating cylinders," J. Fluid Mech. **581**, 221–250 (2007).